Available online at www.sciencedirect.com
ScienceDirect
Trans. Nonferrous Met. Soc. China 33(2023) 3418−3426
Transactions of Nonferrous Metals Society of China
www.tnmsc.cn

# Effect of alloying element Zr on microstructure and properties of Cu−$Y_2O_3$ composites

Yong-qiang QIN[1,2], Yi ZHUANG[1], Lai-ma LUO[1,2,3], Yi-fan ZHANG[1,3], Yu-cheng WU[1,2]

1. School of Materials Science and Engineering, Hefei University of Technology, Hefei 230009, China;
2. National−Local Joint Engineering Research Centre of Nonferrous Metals and Processing Technology, Hefei 230009, China;
3. Engineering Research Center of High Performance Copper Alloy Materials and Processing, Ministry of Education, Hefei 230009, China

Received 29 March 2022; accepted 5 July 2022

**Abstract:** Cu−$Y_2O_3$ and Cu−$Y_2O_3$−Zr composites were prepared via mechanical alloying and spark plasma sintering, and their microstructure and properties were systematically studied by using optical metalloscope, scanning electron microscope, transmission electron microscope, conductivity and tensile tests. It is found that the microstructure of the composites greatly affects mechanical behavior and electrical conductivity. The improvement of electrical property can be attributed to the formation of coherent $Y_4Zr_3O_{12}$ particles and the preferential nucleation of $Cu_4Zr$ phase, which improves the interface between $Y_2O_3$ and Cu matrix, and reduces the dislocation density, respectively. In addition, the Cu−$Y_2O_3$−Zr composites can achieve 265.6 MPa of yield strength, 301.0 MPa of ultimate tensile strength, 23.6% of elongation, and 92.0%(IACS) of electrical conductivity.

**Key words:** Cu−$Y_2O_3$ composites; zirconium; mechanical properties; electrical properties

## 1 Introduction

Dispersion-strengthened copper (DS-Cu) is widely used in heat sink materials and electrical contact materials due to its excellent mechanical properties and electrical conductivity [1]. It is reported that using uniformly distributed nanoparticles (NPs) in DS-Cu can improve the mechanical properties. In recent years, many kinds of NPs such as $Al_2O_3$ [2,3], $Y_2O_3$ [4,5], and $ZrO_2$ [6] have been studied, and $Y_2O_3$ is considered as one of the most competitive candidates due to the higher thermodynamic stability and lower solubility in Cu. Extensive methods have been applied for preparing DS-Cu, such as mechanical alloying (MA) [7,8], wet chemical method [9,10], and internal oxidation method [11−13]. Among them, MA method and spark plasma sintering (SPS) are widely used because of the rapid sintering and higher density of samples.

There is a trade-off between mechanical properties and electronic conductivity within DS-Cu, and great efforts have been made to simultaneously improve the mechanical and electrical properties of DS-Cu. Some studies [14−16] show that the addition of microalloying elements into DS-Cu alloys is a promising solution, which can maintain excellent mechanical properties without compromising conductivity. For example, ZHANG et al [17] found that adding La could lower oxygen content in the alloy and thus decrease its resistivity. ZHOU et al [18] revealed that the involvement of Ti effectively inhibited the coarsening of $Y_2O_3$

**Corresponding author:** Lai-ma LUO, Tel/Fax: +86-551-62905150, E-mail: luolaima@126.com;
Yu-cheng WU, E-mail: ycwu@hfut.edu.cn
DOI: 10.1016/S1003-6326(23)66343-5

particles and improved the alloy's mechanical properties. XU et al [19] found that Zr element enabled the formation of $Y_4Zr_3O_{12}$ particles with $Y_2O_3$ in oxide dispersion-strengthened (ODS) steel, thereby inhibiting the formation of Y−Al−O particles and effectively controlling the structure and size of oxide particles. However, the effect of Zr element on ODS copper has been rarely studied in recent reports.

In this work, Cu−$Y_2O_3$ and Cu−$Y_2O_3$−Zr composites were prepared by MA and SPS methods. The microstructure, mechanical and electrical properties were systematically studied, and the effects of Zr on the mechanical and electrical properties of Cu−$Y_2O_3$ composites were investigated. It is expected that our study will give new insight into the development of high-performance DS-Cu alloy.

## 2 Experimental

### 2.1 Sample preparation

The specific compositions of Cu−$Y_2O_3$ and Cu−$Y_2O_3$−Zr are presented in Table 1. The used raw materials (provided by the Shanghai Linghan Scientific Instrument Co., Ltd.) were pure copper powder (purity ≥99.9%, and average particle size 1 μm), pure zirconium powder (purity ≥99.9%, and average particle size 1 μm), and yttrium oxide powder (purity ≥99.5%, and average particle size 500 nm).

The schematic diagram of the ODS-Cu preparation process is shown in Fig. 1. Cu powder, Zr powder and $Y_2O_3$ powder were pre-mixed at a mass ratio of 98.8:1:0.2, MA was conducted by a QM−QX4 high-energy planetary ball mill under the argon atmosphere, stainless steel milling balls and vials were used, and the milling ball size was 5 mm in diameter. The ball-to-powder mass ratio (BPR), milling speed and milling time were 5:1, 400 r/min and 8 h, respectively. The milled powder was processed with a pressure of 10 MPa at 600 ℃ for 3 min and SPS was performed with a pressure of 50 MPa at 900 ℃ for 5 min.

**Table 1** Compositions of copper matrix composites (wt.%)

| Material | Cu | $Y_2O_3$ | Zr |
|---|---|---|---|
| Cu−$Y_2O_3$ | 99.0 | 1.0 | − |
| Cu−$Y_2O_3$−Zr | 98.8 | 1.0 | 0.2 |

### 2.2 Sample characterization

The surface morphology and microstructure of the composites were observed using metallographic microscope, scanning electron microscope (SEM, SU8020) and transmission electron microscope (TEM, JEM−2100F). The material's density of the sample was measured using the Archimedes drainage method. A D60K digital metal conductivity tester was used to measure the conductivity. Tensile test was carried out using an SS−J3 sample with a displacement rate of 0.3 mm/min at room temperature [20]. The dimensions of the tensile sample used for the tensile test are shown in Fig. 2.

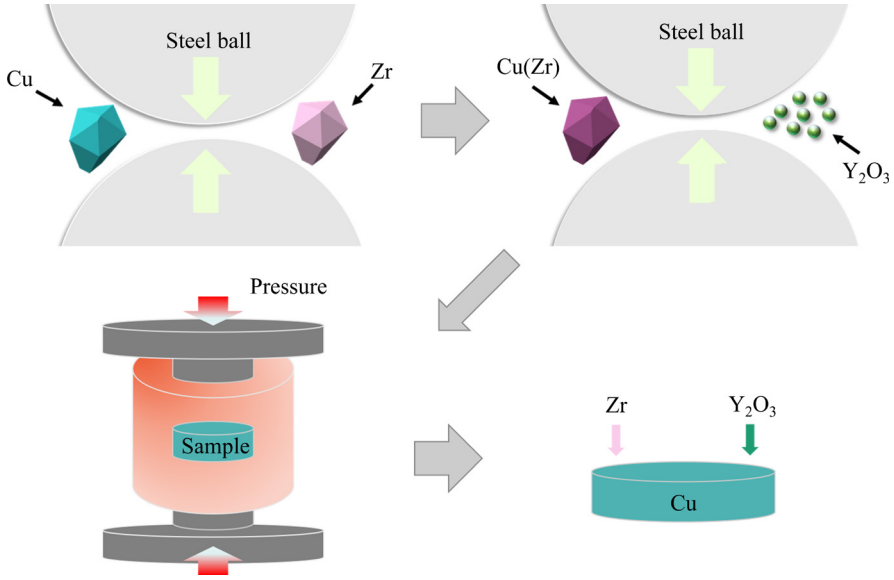


**Fig. 1** Schematic diagram of ODS-Cu preparation process

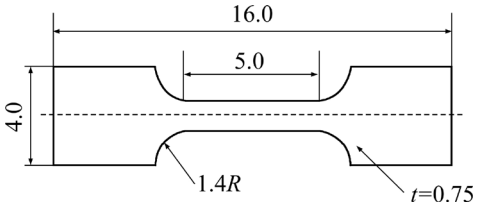


**Fig. 2** Dimensions of tensile samples ($R$ is radius, and $t$ is thickness) (unit: mm)

## 3 Result and discussion

### 3.1 Microstructure

The metallographic images of Cu−$Y_2O_3$ and Cu−$Y_2O_3$−Zr composites are shown in Fig. 3. The grain size of Cu−$Y_2O_3$ composite (Fig. 3(a)) is smaller than that of the Cu−$Y_2O_3$−Zr composite (Fig. 3(b)). The Cu−$Y_2O_3$ composite mainly has striped grains, while with the addition of Zr, isometric grains emerge in Cu−$Y_2O_3$−Zr composite except for striped ones. It is known that smaller grains can increase the grain boundary density, and the grain boundary is regarded as a "barrier" that hinders electron transmission [21].

Figures 4(a) and (b) show the high angle annular dark field (HAADF) images of Cu−$Y_2O_3$ and Cu−$Y_2O_3$−Zr composites, respectively. The uniformly distributed NPs can be identified as $Y_2O_3$ by electron diffraction patterns (the inset of Fig. 4(b),

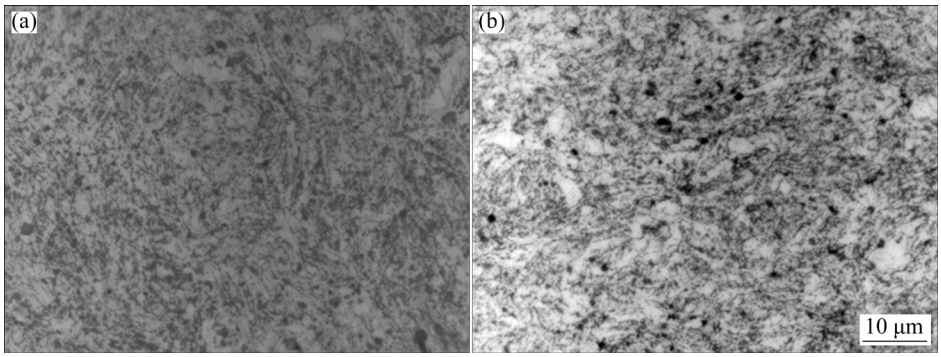


**Fig. 3** Metallographic images of Cu−$Y_2O_3$ (a) and Cu−$Y_2O_3$−Zr (b)

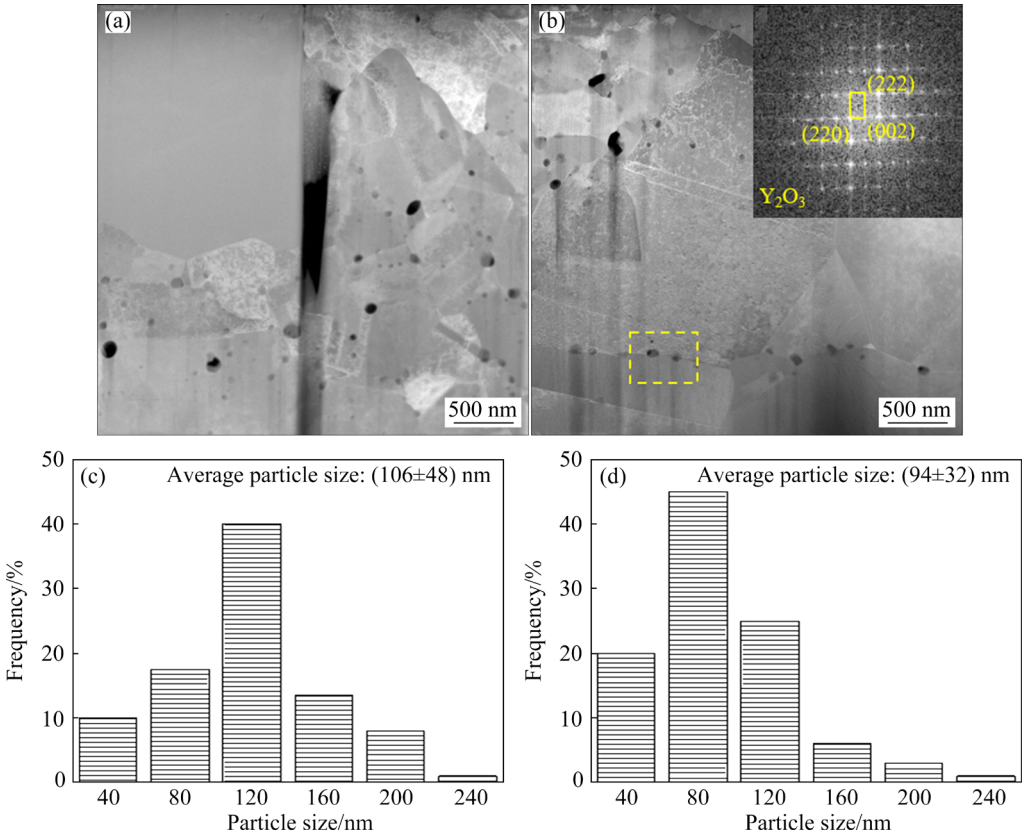


**Fig. 4** STEM HAADF images (a, b) and $Y_2O_3$ particle size distributions (c, d) of Cu−$Y_2O_3$ (a, c) and Cu−$Y_2O_3$−Zr (b, d)

SADP of the yellow area), and most of the $Y_2O_3$ particles in Cu−$Y_2O_3$−Zr composites tend to distribute at the grain boundary. The oxide particle size distribution of Cu−$Y_2O_3$ and Cu−$Y_2O_3$−Zr composites is summarized in Figs. 4(c) and (d), and the size of $Y_2O_3$ nanoparticles in Zr-doped sample is smaller than that in the undoped sample.

Figure 5 shows the TEM dark field image, high-resolution TEM (HRTEM) image and fast Fourier transform (FFT) pattern of Cu−$Y_2O_3$−Zr, indicating the existence of precipitates. In agreement with previous report [22], these precipitates can be identified as $Cu_4Zr$, which has a diameter of about 5 nm. The orientation relationship between Cu and $Cu_4Zr$ is determined as $[1\,\bar{1}\,2]_{Cu}$ // $[20\bar{1}]_{Cu_4Zr}$ and $(1\,\bar{1}1)_{Cu}$ //$(020)_{Cu_4Zr}$, which suggests a coherent or semi-coherent interface.

Figure 6 shows the HRTEM images and corresponding FFT images of $Cu_4Zr$/Cu interface. The FFT images of Area *a* and Area *b* in Fig. 6(a) are shown in Figs. 6(b) and (c), which correspond to $Cu_4Zr$ and $Y_4Zr_3O_{12}$, respectively. $Cu_4Zr$ is distributed around $Y_4Zr_3O_{12}$ with an orientation relationship of $(0\bar{2}0)_{Cu_4Zr}$//$(30\bar{3}\bar{3})_{Y_4Zr_3O_{12}}$. Considering orientation relationship between Cu matrix and $Cu_4Zr$, it is believed that the following orientation relationship

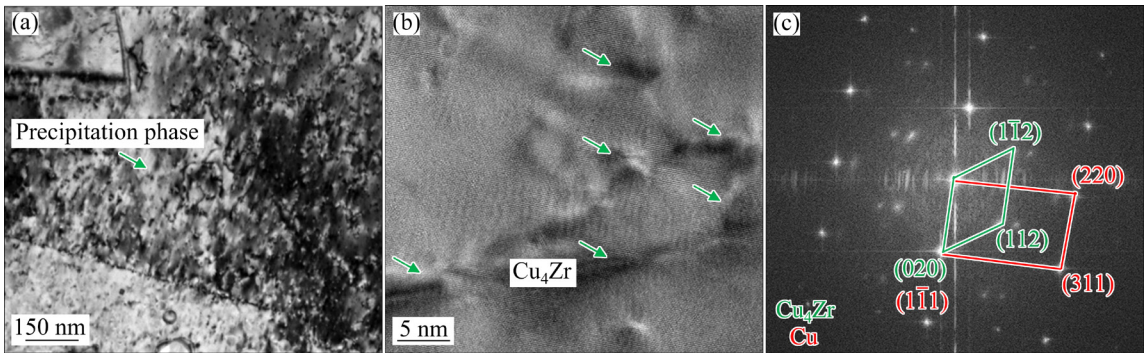


**Fig. 5** TEM dark field image of Cu−$Y_2O_3$−Zr (a), high resolution TEM (HRTEM) image (b), and PPT pattern (c) of Cu−$Y_2O_3$−Zr

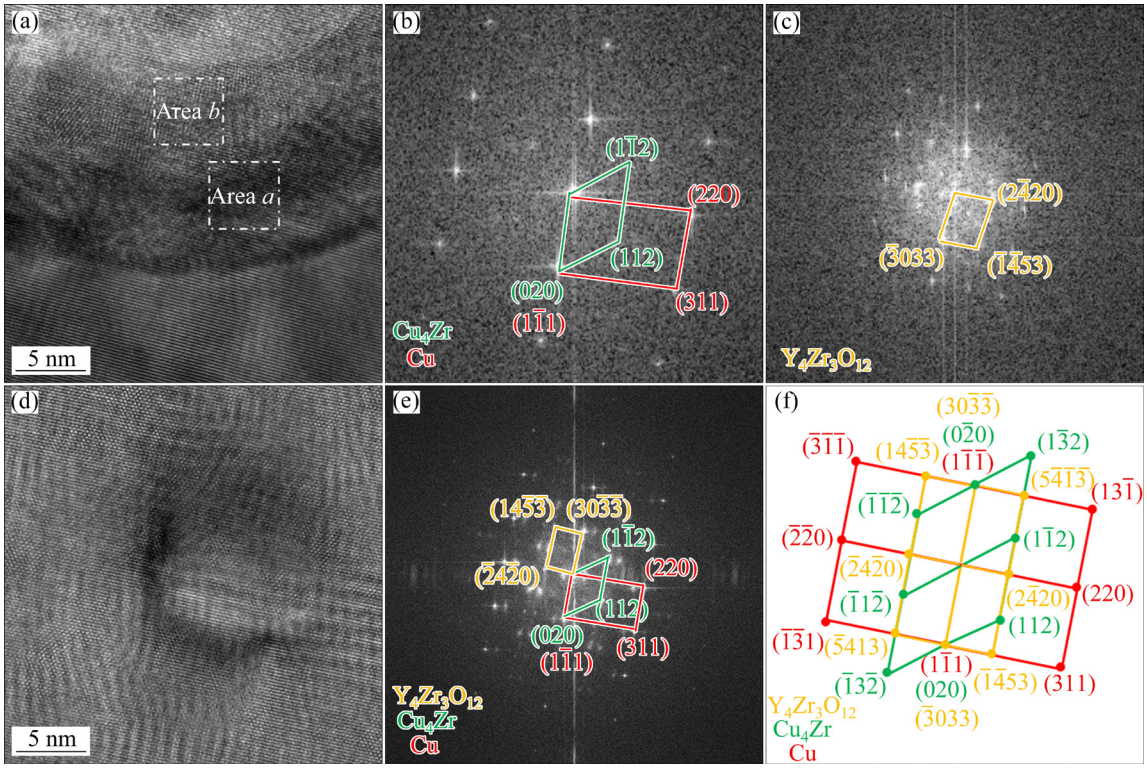


**Fig. 6** HRTEM images of $Cu_4Zr$/Cu interface (a, d), FFT pattern of Area *a* (b), FFT pattern Area *b* (c), FFT pattern (e) of (d), and diagram showing orientation relationship between Cu, $Cu_4Zr$ and $Y_4Zr_3O_{12}$ (f)

between $Y_4Zr_3O_{12}$ and Cu matrix would be $(\bar{1}\bar{1}\bar{1})_{Cu}$ //$(30\bar{3}\bar{3})_{Y_4Zr_3O_{12}}$ and $(2\bar{2}0)_{Cu}$ // $(2420)_{Y_4Zr_3O_{12}}$. These results indicate that the formation of $Y_4Zr_3O_{12}$ phase can reduce the solid dissolved oxygen.

### 3.2 Stacking fault and dislocation density

Figure 7 shows the HRTEM images of Cu−$Y_2O_3$ and Cu−$Y_2O_3$−Zr. As shown in Fig. 7(a), it is clear to see stacking faults parallel to $(\bar{1}11)$ crystal plane. In contrast, no such stacking fault is observed in Cu−$Y_2O_3$. Considering that these stacking faults may be caused by the thermal mismatch between the Cu matrix and the $Y_2O_3$ particles during SPS process, the stacking fault disappears, which implies the stress release mechanism in Cu−$Y_2O_3$−Zr. That is because $Cu_4Zr$ prefers to nucleate along stacking faults in order to reduce distortion energy, and the new $Cu_4Zr$ phase precipitates with the disappearance of stacking faults.

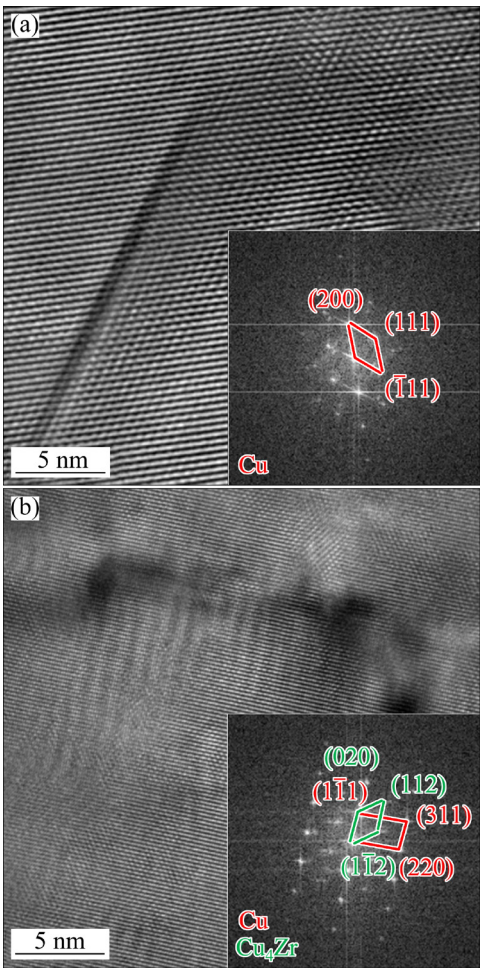


**Fig. 7** HRTEM images and FTT patterns of Cu−$Y_2O_3$ (a) and Cu−$Y_2O_3$−Zr (b)

### 3.3 Mechanical properties

The stress−strain curves from the uniaxial tensile test after SPS are shown in Fig. 8. SS−J3 small tensile samples were used in this work. The yield strength was determined through a bilinear fit procedure [23]. The detailed results of mechanical properties are collected in Table 2. Cu−$Y_2O_3$−Zr has a comparable relative density of 98.6% compared to 98.0% of Cu−$Y_2O_3$. The ultimate tensile strength (UTS, $\sigma_b$) and yield strength (YS, $\sigma_{0.2}$) of the Cu−$Y_2O_3$ composites are 253.0 and 230.1 MPa, respectively. For Cu−$Y_2O_3$−Zr, the UTS and YS values increase to 301.0 and 265.6 MPa, respectively. In addition, the elongation of Cu−$Y_2O_3$ is 17.4%, which increases to 23.6% for Cu−$Y_2O_3$−Zr. These results reveal the improvement of plasticity in Cu−$Y_2O_3$−Zr. Figure 9(a) shows a ductile fracture with ductile dimples of Cu−$Y_2O_3$. Large size dimples with aggregated $Y_2O_3$ particles can be seen at the bottom, which result in the lower interface bonding strength, and the higher interface energy, leading to poor shaping performance [24]. Different from the case of Cu−$Y_2O_3$, the dimple distribution of the Cu−$Y_2O_3$−Zr is relatively uniform (Fig. 9(b)), indicating that the addition of alloying element Zr effectively inhibits the coarsening of $Y_2O_3$.

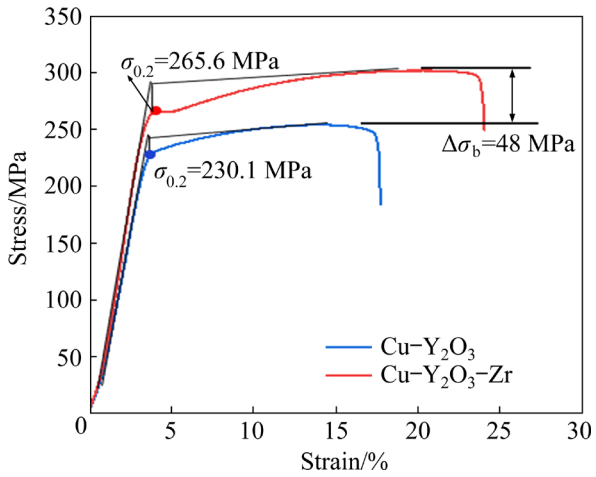


**Fig. 8** Engineering stress−strain curves of Cu−$Y_2O_3$ and Cu−$Y_2O_3$−Zr

**Table 2** Mechanical properties of Cu−$Y_2O_3$ and Cu−$Y_2O_3$−Zr

| Material | Relative density/% | $\sigma_b$/MPa | $\sigma_{0.2}$/MPa | Elongation/% |
|---|---|---|---|---|
| Cu−$Y_2O_3$ | 98.0 | 253.0 | 230.1 | 17.4 |
| Cu−$Y_2O_3$−Zr | 98.6 | 301.0 | 265.6 | 23.6 |

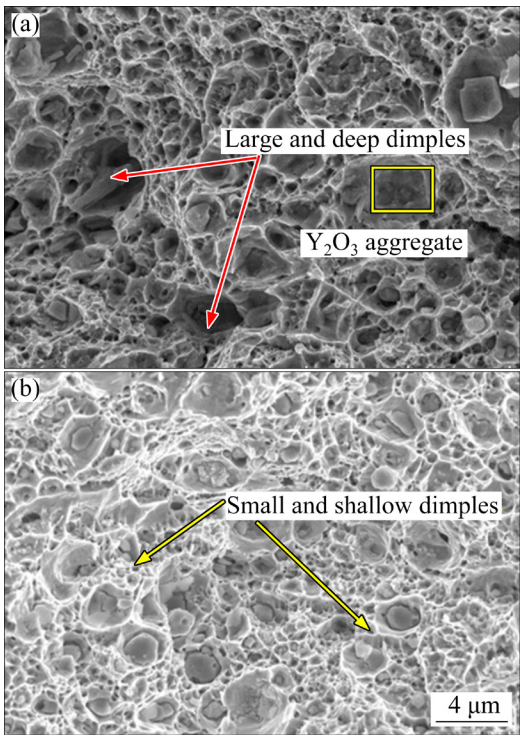


**Fig. 9** Fracture morphologies of Cu−$Y_2O_3$ (a) and Cu−$Y_2O_3$−Zr (b)

As shown in Fig. 4, most of the $Y_2O_3$ particles are distributed at the grain boundaries, which can benefit the grain refinement. According to the Hall−Petch equation, smaller grain sizes can improve UTS. However, the grain size of Cu−$Y_2O_3$ is smaller than that of Cu−$Y_2O_3$−Zr. Hence, the enhancement of YS and UTS for Cu−$Y_2O_3$−Zr is not due to grain refinement. Instead, the second-phase strengthening mechanism plays a significant role in improving the mechanical properties. The second-phase strengthening mechanism is actually divided into dispersion strengthening and precipitation strengthening. The typical dispersion strengthening inside the grains can be described as the Orowan strengthening mechanism, which suppresses the movement of dislocations by adding non-deformable particles. The Orowan strengthening ($\sigma_{\text{Orowan}}$) mechanism can be described as follows:

$$\sigma_{\text{Orowan}} = \frac{0.4Gb}{\pi\sqrt{1-\nu}}\frac{1}{L}\ln\left(\frac{D}{b}\right) \tag{1}$$

where $G$ is the shear modulus, $\nu$ is the Poisson's ratio, $b$ is the amplitude of the Burger vector, $L$ is the average particle spacing, and $D$ is the average particle size. As shown in Fig. 4, the size of $Y_2O_3$ nanoparticles in Cu−$Y_2O_3$−Zr is smaller than that in Cu−$Y_2O_3$, which results in a higher number density of the $Y_2O_3$ nanoparticles in the Cu−$Y_2O_3$−Zr. The fine $Y_2O_3$ nanoparticles are more conductive to pinning dislocations, hindering the movement of dislocations and grain boundary slip, thereby improving the strength of composite. Precipitation strengthening is another mechanism, we can actually observe the $Cu_4Zr$ precipitates in Cu−$Y_2O_3$−Zr (Fig. 5), which also contribute to the enhanced YS and UTS of Cu−$Y_2O_3$−Zr because of the nano-size and high density of formed $Cu_4Zr$ particles.

### 3.4 Electrical conductivity

The electrical conductivity values of Cu−$Y_2O_3$ and Cu−$Y_2O_3$−Zr were 82.1%(IACS) and 92.0% IACS, respectively. The loss of electrical conductivity is widely known to be caused by defects in the material [25], such as dislocation, stacking fault, nanoparticle and grain boundary.

The resistivity change is caused by grain boundaries ($\Delta\rho_{\text{gb}}$), nanoparticles ($\Delta\rho_{\text{p}}$) and dislocations ($\Delta\rho_{\text{dis}}$). The resistivity change ($\Delta\rho_{\text{gb}}$) caused by the grain boundary can be calculated as follows [21]:

$$\Delta\rho_{\text{gb}}=2/3\rho_{\text{sgb}}(S/V) \tag{2}$$

where $\rho_{\text{sgb}}$ is a specific copper grain boundary resistivity, $S$ is the grain boundary surface area, and $V$ is the volume. Considering that the Cu grains in this study are not spherical, the length of the grain boundary per unit area ($\varphi_{\text{gb}}$) is used to characterize the grain boundary density, and $\varphi_{\text{gb}}$ is proportional to $S/V$. The calculation method is as follows [17]:

$$\varphi_{\text{gb}} = K_0\frac{S}{V} = \frac{\sum n_{\text{v}}}{\sum L_{\text{v}}} + \frac{\sum n_{\text{h}}}{\sum L_{\text{h}}} \tag{3}$$

where $L_{\text{v}}$ and $L_{\text{h}}$ are the total lengths of horizontal and vertical lines, respectively; $n_{\text{v}}$ and $n_{\text{h}}$ are the numbers of intersections with the line segment derived from Eqs. (2) and (3) respectively; $\Delta\rho_{\text{gb}}$ is proportional to $\varphi_{\text{gb}}$. Therefore, the larger the grain boundary density is, the lower the electrical conductivity is. $\varphi_{\text{gb}}$ values of Cu−$Y_2O_3$ and Cu−$Y_2O_3$−Zr are listed in Table 3. According to this result, we can conclude the improvement of the conductivity of Cu−$Y_2O_3$−Zr is relative to the decrease in grain boundary density.

**Table 3** Grain boundary density and electrical resistivity of $Cu–Y_2O_3$ and $Cu–Y_2O_3–Zr$

| Material | $\varphi_{gb}/m^{-1}$ | Electrical resistance/ $10^{-8}\Omega$ |
|---|---|---|
| $Cu–Y_2O_3$ | 5.63 | 2.09 |
| $Cu–Y_2O_3–Zr$ | 4.52 | 1.87 |

The $\Delta\rho_p$ is mainly determined by the volume fraction of doped nanoparticles in the matrix. The volume fraction of $Y_2O_3$ nanoparticles in this work is about 1.75% for both composites, suggesting a similar contribution of nanoparticles. However, the shape and the size of the nanoparticles have great impact on the conductivity. ZENG et al [26] developed an alternative to Norbury–Linderule by an effective pattern recognition application and investigated the effects of 79 elements on the conductivity of Cu, and they found that Zr had detrimental effect on the conductivity of Cu. In our prepared $Cu–Y_2O_3–Zr$, the formation of $Cu_4Zr$ reduces the content of solute Zr, which greatly eliminates the negative impact of Zr on the conductivity.

The coherent/semi-coherent interface of Cu matrix and $Y_4Zr_3O_{12}$ phase is another reason [27]. Due to its better interface bonding, the scattering effect of coherent $Y_4Zr_3O_{12}$ nanoparticles on electrons is weaker than that of non-coherent $Y_2O_3$ nanoparticles, leading to a relatively high conductivity [18]. The formation of $Y_4Zr_3O_{12}$ particles reduces the oxygen content in the Cu matrix and thus improves the electrical properties of the $Cu–Y_2O_3$ composite [28]. As reported, uniform distribution caused by the coherent/semi-coherent interface is beneficial to improving conductivity and plasticity [17]. This may be the reason why the elongation of $Cu–Y_2O_3–Zr$ is also increased slightly.

The resistivity change caused by dislocations ($\Delta\rho_{dis}$) is proportional to the number of dislocations [29]. $Cu_4Zr$ and $Y_4Zr_3O_{12}$ can fill stacking faults, which reduces dislocation density and improves electrical conductivity. Therefore, the formation of coherent $Y_4Zr_3O_{12}$ phase and the decrease of both grain boundary density and dislocation density are responsible for the reduced internal defects of $Cu–Y_2O_3$ after the introduction of Zr alloying element.

## 4 Conclusions

(1) The doped Zr element enables the formation of $Y_4Zr_3O_{12}$ particles and coherent precipitate-phase $Cu_4Zr$.

(2) Fine $Cu_4Zr$ and $Y_4Zr_3O_{12}$ particles improve the mechanical properties of the composite.

(3) The formation of coherent $Y_4Zr_3O_{12}$ phase and the decrease of both grain boundary density and dislocation density facilitate the better electrical conductivity.

(4) The addition of Zr can improve the comprehensive properties of the $Cu–Y_2O_3–Zr$ composite, with 265.6 MPa of yield strength, 301.0 MPa of ultimate tensile strength, 23.6% of elongation, and 92.0%(IACS) of electrical conductivity.

## Acknowledgments

This work was supported by the National Key Research and Development Program of China (No. 2019YFE03120002), the Natural Science Foundation of Anhui Province, China (Nos. 2108085J21, S202202a04021990), the National Key Research and Development Program of Anhui Province, China (No. 202103a05020002), and the Higher Education Discipline Innovation Project (No. B18018).

## References

[1] QIN Yong-qiang, TIAN Yu, PENG Yu-qiang, LUO Lai-ma, ZAN Xiang, XU Qiu, WU Yu-cheng. Research status and development trend of preparation technology of ceramic particle dispersion strengthened copper−matrix composites [J]. Journal of Alloys and Compounds, 2020, 848: 156475.

[2] LIN Huan-ran, GUO Xiu-hua, SONG Ke-xin, FENG Jiang, LI Shao-lin, ZHANG Xiang-feng. Synergistic strengthening mechanism of copper matrix composite reinforced with nano-$Al_2O_3$ particles and micro-SiC whiskers [J]. Nanotechnology Reviews, 2021, 10: 62−72.

[3] XIAO Zhu, HUANG Yin-jie, CHEN Chun-xiang, LI Zhou, GONG Shen, HUANG Yi-xin, ZHANG Chen, ZHANG Xiao-xuan. Effects of thermal treatments on the residual stress and micro-yield strength of $Al_2O_3$ dispersion strengthened copper alloy [J]. Journal of Alloys and Compounds, 2019, 781: 490−495.

[4] DONG Yu, WANG Xin-kai, XIE Yu-huang, YANG Chao, ZHOU Deng-shan. Tunable microstructures and tensile mechanical properties of oxide-dispersion-strengthened Cu by extrusion and secondary processing [J]. Journal of Alloys

and Compounds, 2020, 812: 152112.

[5] CARRO G, MUÑOZ A, MONGE M A, SAVOINI B, PAREJA R, BALLESTEROS C, ADEVA P. Fabrication and characterization of $Y_2O_3$ dispersion strengthened copper alloys [J]. Journal of Nuclear Materials, 2014, 455: 655−659.

[6] MARWA E, GAMAL A, ASAAD A E M. Microstructure and properties of Cu−$ZrO_2$ nanocomposites synthesized by in situ processing [J]. Materials Research, 2017, 21(1): e20170387.

[7] HUANG B, YOSHIMITSU H, HIROYUKI N, TAKEO M. Mechanochemical processing of Cu−$Y_2O_3$ alloy by MA-HIP for heat sink materials application [J]. Fusion Engineering and Design, 2019, 140: 33−40.

[8] HUANG Fei, WANG Hang, YANG Bin, LIAO Tao, WANG Zhao-yang. Uniformly dispersed $Y_2O_3$ nanoparticles in nanocrystalline copper matrix via multi-step ball milling and reduction process [J]. Materials Letters, 2019, 242: 119−122.

[9] QIN Yong-qiang, TIAN Yu, ZHUANG Yi, LUO Lai-ma, ZAN Xiang, WU Yu-cheng. Effects of solid–liquid doping and spark plasma sintering on the microstructure and mechanical properties of $Y_2O_3$-doped copper matrix composites [J]. Vacuum, 2021, 192: 110436.

[10] QIN Yong-qiang, PENG Yu-qiang, TIAN Yu, LUO Lai-ma, MA Yong, ZAN Xiang, ZHU Xiao-yong, WU Yu-cheng. Effect of $Y_2O_3$ on microstructure and mechanical properties of WC−Co-cemented carbides prepared via solid−liquid doping method and spark plasma sintering [J]. Materials Today Communications, 2020, 24: 101096.

[11] YAN Zhi-qiao, CHEN Feng, YE Fu-xing, ZHANG Dong-ping, CAI Yi-xiang. Microstructures and properties of $Al_2O_3$ dispersion-strengthened copper alloys prepared through different methods [J]. International Journal of Minerals, Metallurgy, and Materials, 2016, 23: 1437−1443.

[12] ZHENG Run-guo, LI Na-na. Microstructure and wear properties of Cu−$La_2O_3$ composites prepared by spark plasma sintering [J]. Metals and Materials International, 2021, 27: 1103−1112.

[13] MA B, YOSHIMITSU H, YUSUKE S, HIROYUKI N, RYUTA K, NAOKO O, SHIGEHARU U, TAKEO M. The size dependence of microstructure and hardness on the MA powders for the MA-HIP processed Cu−$Y_2O_3$ dispersion-strengthened alloys [J]. Nuclear Materials and Energy, 2020, 24: 100773.

[14] ZHANG Xiu-zhen, JIN Shen-bao, YANG Chao, ZHOU Deng-shan, SHA Gang, ZHANG De-liang. Enhanced tensile properties in a Cu−$Al_2O_3$ alloy via trace Ti addition [J]. Journal of Alloys and Compounds, 2021, 862: 158687.

[15] YANG Jing-zhao, BU Kun, SONG Ke-xing, ZHOU Yang-jun, HUANG Tao, NIU Li-ye, GUO Hui-wen, DU Yi-bo, KANG Jun-wei. Influence of low-temperature annealing temperature on the evolution of the microstructure and mechanical properties of Cu−Cr−Ti−Si alloy strips [J]. Materials Science and Engineering A, 2020, 789: 140120.

[16] LI Ming-yang, HU Pei, ZHANG Yi-ming, CHANG Yong-qin. Enhancing performance of the CuCrZrTiV alloys through increasing recrystallization resistance and two-step thermomechanical treatments [J]. Journal of Nuclear Materials, 2021, 543: 152482.

[17] ZHANG Yi-fan, JI Zhen, JIA Cheng-chang, LIU Gui-min, WAN Fa-rong, ZHAN Qian. Influence of lanthanum on enhancement of mechanical and electrical properties of Cu−$Al_2O_3$ composites [J]. Journal of Rare Earths, 2019, 37: 534−540.

[18] ZHOU Deng-shan, WANG Xin-kai, ZENG Wei, YANG Chao, PAN Hu-cheng, LI Cheng-guang, LIU Yu-jie, ZHANG De-liang. Doping Ti to achieve microstructural refinement and strength enhancement in a high volume fraction $Y_2O_3$ dispersion strengthened Cu [J]. Journal of Alloys and Compounds, 2018, 753: 18−27.

[19] XU Hai-jian, LU Zheng, WANG Dong-mei, ZHANG Zhi-wei, LIU Chun-ming. Structure and composition of oxides in FeCrAl ODS alloy with Zr addition [J]. Materials Science and Technology, 2017, 33: 1790−1795.

[20] TAKASHI N, HIDEO S, CHEN X, TAICHIRO K, JOSINA W G, YUTAI K, HIROYASU T. Non-contact strain evaluation for miniature tensile specimens of neutron-irradiated F82H by digital image correlation [J]. Fusion Engineering and Design, 2020, 157: 111663.

[21] ANDREWS P V, WEST M B, ROBESON C R. The effect of grain boundaries on the electrical resistivity of polycrystalline copper and aluminium [J]. Philosophical Magazine, 1969, 19: 887−898.

[22] LI G Y, LI S Y, LI L, ZHANG D T, WANG J D, TONG Y X. A high strength and high electrical conductivity CuCrZr alloy prepared by aging and subsequent cryorolling [J]. Vacuum, 2021, 190: 110315.

[23] ALTSYADT E, GE H E, KUKSENKO V, CRITICAL M. Evaluation of the small punch test as a screening procedure for mechanical properties [J]. Journal of Nuclear Materials, 2016, 472: 186−195.

[24] LU Tian-xing, CHEN Cun-guang, LI Pei, ZHANG Chen-zeng, HAN Wei-hao, ZHOU Yang, CHALLAPALLI S, GUO Zhi-meng. Enhanced mechanical and electrical properties of in situ synthesized nano-tungsten dispersion-strengthened copper alloy [J]. Materials Science and Engineering A, 2021, 799: 140161.

[25] LIAO Heng-cheng, WU Yu-na, WANG Yong-jin. Microstructure evolution of Al−0.35%Si−0.2%Mg−0.3%Ce alloy during hot extrusion and its contributions to performances [J]. Journal of Materials Engineering and Performance, 2015, 24: 2503−2510.

[26] ZENG Ying-zhi, MU Shen-jing , WU Ping, KHUONG P O, ZHANG Jia. Relative effects of all chemical elements on the electrical conductivity of metal and alloys: An alternative to Norbury–Linderule [J]. Journal of Alloys and Compounds, 2009, 478: 345−354.

[27] WU You, ZHAO Hao-zhi, LI Jing-kang, ZHANG Yuan-yuan, LIU Tong. Effects of $Y_4Zr_3O_{12}$ addition on the microstructure and mechanical properties of Fe−15Cr−2W−0.35Ti ODS steels [J]. Materials Science and Engineering A, 2021, 804: 140734.

[28] CAO Guo-qin, YANG Lei, YUAN Gai-huan, HU Jun-hua, SHAO Guo-sheng, YAN Long. Chemical diversity of iron

species and structure evolution during the oxidation of C14 Laves phase $Zr(Fe,Nb)_2$ in subcritical environment [J]. Corrosion Science, 2020, 162: 108218.

[29] SCHAFLER E, STEINER G, KORZNIKOVA E, KERBER M, ZEHETBAUER M J. Lattice defect investigation of ECAP-Cu by means of X-ray line profile analysis, calorimetry and electrical resistometry [J]. Materials Science and Engineering A, 2005, 410/411: 169−173.

# 合金元素 Zr 对 Cu−$Y_2O_3$ 复合材料组织和性能的影响

秦永强[1,2]，庄 翌[1]，罗来马[1,2,3]，张一帆[1,3]，吴玉程[1,2]

1. 合肥工业大学 材料科学与工程学院，合肥 230009；
2. 有色金属与加工技术国家地方联合工程研究中心，合肥 230009；
3. 高性能铜合金材料及成形加工教育部工程研究中心，合肥 230009

**摘 要：**通过机械合金化和放电等离子烧结制备 Cu−$Y_2O_3$ 和 Cu−$Y_2O_3$−Zr 复合材料，并采用光学显微镜、扫描电镜、透射电镜、电导率和拉伸实验对其组织和性能进行系统研究。研究发现，复合材料的显微组织对其力学性能和电导率具有很大影响。电学性能的改善可归因于共格 $Y_4Zr_3O_{12}$ 粒子的形成和 $Cu_4Zr$ 相的优先成核，它们分别改善了 $Y_2O_3$ 和 Cu 基体之间的界面以及降低了位错密度。此外，Cu−$Y_2O_3$−Zr 复合材料的屈服强度为 265.6 MPa，极限抗拉强度为 301.0 MPa，伸长率为 23.6%，电导率达到 92.0% (IACS)。

**关键词：**Cu−$Y_2O_3$ 复合材料；锆；力学性能；电学性能

**(Edited by Wei-ping CHEN)**